www.sciencemag.org/cgi/content/full/science.1232322/DC1

Supplementary Materials for

Structure of the Repulsive Guidance Molecule (RGM)–Neogenin Signaling Hub

Christian H. Bell, Eleanor Healey, Susan van Erp, Benjamin Bishop, Chenxiang Tang, Robert J. C. Gilbert, A. Radu Aricescu, R. Jeroen Pasterkamp, Christian Siebold*

*Corresponding author. E-mail: christian@strubi.ox.ac.uk

Published 6 June 2013 on *Science* Express
DOI: 10.1126/science.1232322

This PDF file includes:

Supporting Online Material for

"Structure of the Repulsive Guidance Molecule (RGM)-Neogenin signalling hub"

Christian H. Bell[1#], Eleanor Healey[1+], Susan van Erp[2+], Benjamin Bishop[1], Chenxiang Tang[1*], Robert J.C. Gilbert[1], A. Radu Aricescu[1], R. Jeroen Pasterkamp[2], & Christian Siebold[1†]

[1]Division of Structural Biology, Wellcome Trust Centre for Human Genetics, University of Oxford, Roosevelt Drive, Oxford OX3 7BN, United Kingdom.

[2]Department of Neuroscience and Pharmacology, Rudolf Magnus Institute of Neuroscience, University Medical Center Utrecht, CG Utrecht 3584, The Netherlands.

[#]Current address: Roche Diagnostics GmbH, Nonnenwald 2, 82377 Penzberg, Germany.

[*]Current address: Molecular Biophysics and Biochemistry Dept., Yale University, 260 Whitney Avenue, New Haven, CT 06520-8114, USA.

[+]These authors contributed equally.

[†]To whom correspondence should be addressed. E-mail: christian@strubi.ox.ac.uk.

This PDF file includes:

Materials and Methods

Expression and purification of RGM, NEO1 and DCC constructs and complexes. Constructs of the extracellular region of human RGMA (GenBank ID AL136826; eRGMA: 47-423), human RGMB (GenBank ID AK074887, eRGMB: 53-412), human RGMC (GenBank ID AY372521; eRGMC: 36-400), mouse NEO1 (GenBank ID Y09535; $NEO1_{FN56M}$: 883-1134, $NEO1_{FN56}$: 883-1083 and eNEO1: 37-1134) and human DCC (GenBank ID AC011155; eDCC: 26-1129), as well as a full-length transmembrane construct of mouse NEO1 (fNEO1: 37-1493), fused C-terminally with a hexa-histidine (His6) tag, a C-terminal BirA recognition sequence or a 1D4 epitope-tag that can bind selectively the Rho 1D4 antibody(30), were cloned into the pHLsec or pHL-Avitag3 vectors(31) and expressed by transient transfection in HEK-293T cells (using an automated procedure(32) in the presence of the class I α-mannosidase inhibitor, kifunensine, as described in(33)). Five days post-transfection, the conditioned medium was dialysed (for 48 hours at 4°C) and the proteins were purified by immobilised metal-affinity chromatography using TALON beads (Clontech) and treated with endoglycosidase F1 (75 μg mg^{-1} protein, 12 h, 21 ºC) to cleave glycosidic bonds of N-linked sugars resulting in only one N-acetyl-glucosamine moiety bound to the corresponding asparagine side chain. The proteins were concentrated and further purified by size-exclusion chromatography (Superdex 200 16/60 column, GE Healthcare) in buffer containing 10mM HEPES, pH 7.5, 150 mM NaCl.

The eRGMB-NEO1 complexes were formed by mixing a molar ratio of 1:1. The mixture was incubated for 1 h at room temperature and purified by size-exclusion chromatography (Superdex 200 16/60 column, GE Healthcare) in buffer containing 10 mM HEPES, pH 7.5, 150 mM NaCl.

Site directed mutagenesis. Site-directed mutagenesis to test specificity of protein-protein interactions or to stabilise the ectodomain of human RGMC (eRGMC$_{AAA}$: R326A/R329A/R332A) was carried out following a two-step, overlap-extension PCR using Pyrobest Polymerase (Takara). PCR products were cloned into the pHLsec or pHL-Avitag3 vectors resulting in protein constructs with a C-terminal hexa-histidine or with a C-terminal BirA recognition sequence(31). Mutant proteins were secreted at similar levels to the respective wildtype RGM and NEO1 constructs (data not shown). The stringent quality control mechanisms specific to the mammalian cell secretory pathway is likely to ensure that secreted proteins are correctly folded(34).

Crystallization and data collection. Protein samples were concentrated in size exclusion chromatography buffer by ultrafiltration to appropriate concentrations for crystallization experiments (NEO1$_{FN56}$: 10 mg/ml, eRGMB-NEO1$_{FN56}$: 7 mg/ml). Nanolitre crystallization trials using a Cartesian Technologies robot (100 nl protein solution plus 100 nl reservoir solution) were setup in 96-well Greiner plates, placed in a TAP (The Automation Partnership) Homebase storage vault maintained at 295 K and imaged via a Veeco visualization system(35). NEO1$_{FN56}$ Form 1 crystals were grown out of a mother liquor containing 0.1 M Tris-HCl, pH 8.5, 0.2 M sodium acetate, 30% PEG4000, NEO1$_{FN56}$ Form 2 crystals out of mother liquor containing 0.13 M potassium nitrate, 13% PEG3350, eRGMB-NEO1$_{FN56}$ Form 1 crystals out of mother liquor containing 0.1 M Tris Propane, pH 8.5, 0.2 M potassium nitrate, 20% PEG3350, eRGMB-NEO1$_{FN56}$ Form 2 crystals out of mother liquor containing 0.1 M Tris-HCl, pH 8.5, 0.2 M lithium sulphate, 25% PEG3350 and eRGMB-NEO1$_{FN56}$ Form 3 crystals out of mother liquor containing 0.1 M sodium acetate, pH 4.6, 0.18 M potassium acetate, 18% PEG3350. For the NEO1$_{FN56}$-sucrose octasulphate (SOS) complex

$NEO1_{FN56}$ was mixed with 3 mM SOS prior to crystallization and crystals were grown out of mother liquor containing 0.15 M potassium nitrate, 15% PEG3350.

Diffraction data were collected at 100 K. Prior to flash-freezing, crystals were treated with the appropriate cryo protectant solutions ($NEO1_{FN56}$ Form 1, $NEO1_{FN56}$ Form 2 and eRGMB-$NEO1_{FN56}$ Form 1: 25% (v/v) glycerol in mother liquor; eRGMB-$NEO1_{FN56}$ Form 2, eRGMB-$NEO1_{FN56}$ Form 3 and $NEO1_{FN56}$-SOS: 28% (v/v) ethylene glycol in mother liquor). Data were collected at beamline I03 (eRGMB-$NEO1_{FN56}$ Form 1, 2 and 3 and $NEO1_{FN56}$ Form 2) at the Diamond Light Source, UK (equipped with a Pilatus 6M-F detector) and at beamline ID14-EH4 ($NEO1_{FN56}$-SOS and $NEO1_{FN56}$ Form 1) at the European Synchrotron Radiation Facility (ESRF), France (equipped with an ADSC Q315r detector). X-ray data were processed and scaled with the HKL suite(36) and XIA2(37). Data collection statistics are shown in table S1.

Structure determination and refinement. The eRGMB-$NEO1_{FN56}$ Form 3 complex was solved by molecular replacement in PHASER(38) using the structure of the fifth and sixth FNIII domain of human NEO1 (PDB ID: 3P4L(39)) as search model. Additional electron density for RGMB was immediately discernible. After density modification with PARROT as implemented in CCP4i(40) (figS1 A, B), the RGMB polypeptide chain was traced using Buccaneer(40). Iterative rounds of refinement in autoBUSTER(41), PHENIX(42), chain tracing in BUCCANEER(40) and manual building in COOT(43) resulted in a well-defined model for human RGMB that included residues 134-338 (Fig. 1B). The RGMB N- and C-terminal regions and the loop region between residues 143 and 157 could not be traced due to missing electron density and were thus not included in the final model. All other structures were solved by molecular replacement in PHASER using the refined RGMB and NEO1 chains of the eRGMB-$NEO1_{FN56}$ Form 3 complex. The models were refined using programs

autoBUSTER(41) and PHENIX(42) and, where applicable, non-crystallographic symmetry restraints were used. As the test sets for all structures were chosen randomly the presence of non-crystallographic symmetry may artificially lower the value of Rfree by a small amount but will not render the metric invalid(44). The low resolution eRGMB-NEO1$_{FN56}$ Form 2 complex structure was refined in PHENIX(42) only applying rigid body and TLS refinement. The resulting electron density maps are of reasonable quality and clearly show features, which are not present in the model used for molecular replacement (fig. S1D-F). Crystallographic and Ramachandran statistics are given in tableS1. Stereochemical properties were assessed by MOLPROBITY(45). Superpositions were calculated using the program SHP(46) and COOT(43) and electrostatic potentials were generated using APBS(47). Buried surface areas of protein-protein interactions were calculated using the PISA webserver(48) for a probe radius of 1.4 Å.

Multiangle light scattering (MALS). MALS experiments were carried out using a DAWN HELEOS II from Wyatt Technology (equipped with a K5 flow cell and a 30 mW linearly polarized GaAs laser with a wavelength of 690 nm). Proteins used for MALS contained wildtype sugars. Prior to the experiments, proteins were purified by size exclusion chromatography and concentrated to approximately 2 mg/ml. Data were analysed using ASTRA (Wyatt Technologies) and molecular weights were calculated using the Debye fit method.

Surface plasmon resonance (SPR) binding studies. SPR experiments were performed using a Biacore T100 machine (GE Healthcare) at 25 °C in SPR running buffer (10 mM HEPES, pH 7.4, 150mM NaCl, 0.05% (v/v) polysorbate 20). All experiments were carried out using orientated protein immobilization by coupling biotinylated proteins to streptavidin-

coated biosensor chips(49). Proteins for surface attachment were engineered with a C-terminal recognition sequence for the enzyme BirA, allowing enzymatic biotinylation of a lysine residue within this sequence. Biotinylation of the C-terminus of NEO1 and RGMs replaces the transmembrane helix or the GPI-anchor, respectively, recapitulating the native topology of both proteins. Tagged proteins were secreted from HEK-293T cells with equivalent efficiency to their untagged counterparts. Proteins used as analytes were prepared as described above and underwent gel filtration in running buffer immediately prior to use. Experiments with the wildtype proteins were performed in both orientations and with the mutant proteins in one orientation. Protein concentrations were determined from the absorbance at 280 nm using calculated molar extinction coefficients. Typically the ligands were bound to the surface at concentrations of 150-3,000 response units. After each binding experiment the chip was regenerated by short bursts of 2 M Magnesium sulphate. All experiments were done in duplicates with independently purified proteins. In all experiments analyzed, the experimental trace returned to baseline after each injection and the data fitted to a simple 1:1 Langmuir model of binding. K_d values were obtained by nonlinear curve fitting of the Langmuir binding isotherm (bound = $C^*max/(K_d + C)$, where C is analyte concentration and max is the maximum analyte binding) using the Biacore Evaluation software (GE Healthcare).

Analytical ultracentrifugation. Sedimentation velocity (SV) experiments were performed using a Beckman Optima XL-I analytical centrifuge and a run temperature of 20 °C. After gel filtration protein samples were concentrated to the following concentrations for SV analysis: eRGMB-WT and eRGMB-P206N: 3 mg/mL, $NEO1_{FN56M}$: 2 mg/mL and for the complexes, the proteins were mixed in a 1:1 ratio with a final concentration of 6 mg/mL. For the pH-dependent experiments, runs were conducted at pH 7 and pH 4. The samples were held in 3

mm path length Epon sector-shaped 2-channel centrepieces and were spun at 40,000 rpm, with 50 sample distribution scans being taken increments of 6 minutes apart. Data were collected using 280 nm absorbance optics. Data were analysed using Sedfit (*50,51*), available from http://www.analyticalultracentrifugation.com. The scans 6-50 were used in the continuous c(s) distribution analysis, they were performed with a floating frictional ratio and baseline, s_{min} = 0.5, s_{max} = 10, and a resolution of 100. A value of 0.73 ml/g was used for the partial specific volumes. Graphs were plotted and Gaussian distributions fitted to the curves using the plotting program PROFIT (Uetikon am See, Switzerland).

Co-immunoprecipitation

Transfection and co-transfection of full-length fNEO1-His6 and fNEO-1D4 plasmids were performed using previously described methods(31). About 40 hours post-transfection the media (250 ml) was removed. The cells were washed in 2 x 50 mL PBS and lysed in 5 mL Lysis Buffer (10 mM Tris-HCl (pH 8.0), 150 mM NaCl, 1.5% DDM and protease inhibitor cocktail (Sigma)) for 2 hours at 4 °C. The lysate was cleared by centrifugation (100000 xg, 2 hours) and diluted 1:50 in lysis buffer containing 0.03 % DDM. Complexes were recovered on 1D4-antibody (University British Colombia)-conjugated sepharose beads (Amersham) and washed three times with lysis buffer (0.03 % DDM). Bound protein complexes were eluted from the beads by incubation (12 hours, 4 °C) with 500 µM 1D4 peptide (TETSQVAPA, GenScript). Samples were analysed by Western blotting with a mouse anti-His6 antibody probe.

Neurite growth assays. Cerebellar external granule layer (EGL) explants were grown on RGMB coated coverslips. First, coverslips were coated with poly-D-lysine (100 µg/ml), washed and air-dried. Purified RGMB-WT, RGMB-P206N, RGMB-A186R or Fc control protein was then added to the coverslip at 50 µg/ml mixed with laminin (40 µg/ml,

Invitrogen) in Neurobasal medium (NB, Gibco) overnight at 4 °C. Routinely, a 10% adsorption of input protein to poly-D-lysine-coated coverslips was observed(52). Shortly before plating the explants, coverslips were washed once in NB and incubated at 37 °C with culture medium (NB with penicillin/streptomycin, l-glutamine, 18 mM Hepes and 1xB27). Explants were obtained from postnatal day (P)9 mouse pups. In brief, the cerebellum was removed and dissected in ice cold L15, and coronal slices were cut using a MCIllwain tissue chopper. Slices were further dissected to isolate the EGL and equally sized tissue explants were cut and placed onto the coated coverslips. After 3 days *in vitro* (DIV), the explants were fixed with 4% PFA for 20 min at room temperature. For immunohistochemistry, coverslips were washed with PBS and incubated in blocking buffer (PBS with 5% normal goat serum, 1% BSA, 1% glycine, and 0.4% Triton-X100) for 1 hour at RT. Primary (mouse anti βIII-tubulin, T8660 Sigma) and secondary (goat anti mouse Alexa-488, A11029 Molecular Probes) antibodies were diluted in blocking buffer and incubated overnight at 4 °C. Nuclei and F-actin were stained using DAPI (Invitrogen) and Phalloidin-TRITC (Sigma-Aldrich), respectively, diluted in PBS. Pictures were taken with a Zeiss Scope A1 microscope with a 10x objective (Zeiss) and an Axiocam Mrm camera (Zeiss). Neurite outgrowth from the explants was analysed using ImageJ. The distance between explant and the growth cones of > 20 individual, non-fasciculated neurites was measured (three separate experiments, total explants analyzed per condition: WT n=27, P206N n=24, A186R n=26, control n=23) (fig. S13) and neurite lengths were normalized to the average neurite length of control explants per experiment. Three bins (short, medium, long) containing an equal proportion of measurements ranging from shortest to longest were created to establish the distribution of neurite lengths per explant. The percentage of neurites in each bin was calculated for each explant to obtain the average distribution of neurite lengths per condition. A two-way

ANOVA with Bonferroni post-test was used to compare the distributions of neurite length between the experimental conditions.

Illustrations. Figures were produced using the programs PYMOL (www.pymol.org), Adobe Photoshop (Adobe Systems) and Corel Draw (Corel Corporation).

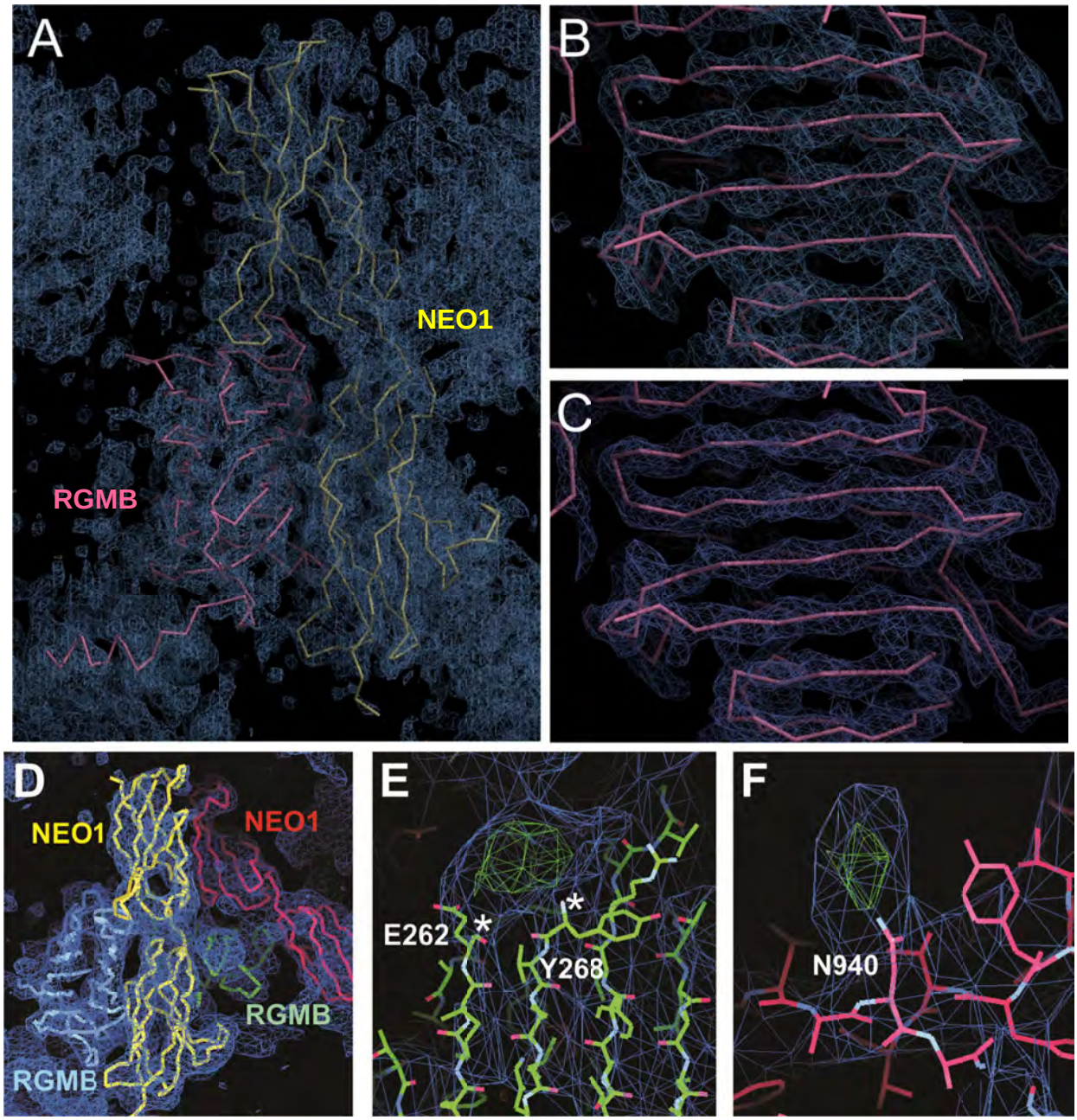

Fig. S1: Electron density of the RGMB-NEO1 complex. (A) Initial electron density map of the low pH (Form 3) eRGMB-NEO1$_{FN56}$ complex contoured at 1.4 σ after molecular replacement in PHASER(38) (using the NEO1$_{FN56}$ structure (pdb 3P4L(39)) as search model) and density modification using PARROT(40). The additional electron density for the RGMB is clearly visible. The final model of the eRGMB-NEO1$_{FN56}$ complex is represented as ribbon with RGMB in pink and NEO1$_{FN56}$ in yellow. The orientation is similar to Fig. 2A. **(B,C)** Detailed view onto one side of the RGMB β-sandwich. **(B)** Initial electron density map as described in (A). **(C)** SigmaA-weighted $2F_O$-F_C map of the final model from autoBUSTER(41) contoured at 1.4 σ. **(D-F)** SigmaA-weighted $2F_O$-F_C map (blue, 1.1 σ) and F_O-F_C map (green, +3.0 σ) from PHENIX(42) after rigid body and TLS refinement of the 6.6 Å neutral pH (Form 2) eRGMB-NEO1$_{FN56}$ complex. **(D)** Overview of the eRGMB-NEO1$_{FN56}$ asymmetric unit. **(E)** Close-up on the previously disordered RGMB loop between residues E262 and Y268. (F) Close-up on the NEO1 N-linked glycosylation site at residue N940, which was excluded from the molecular replacement model. Additional features are clearly visible in the resulting electron density maps, e.g. the RGMB loop region spanning from residues 263-267 (E) as well as the NEO1 N-linked sugar moiety (F).

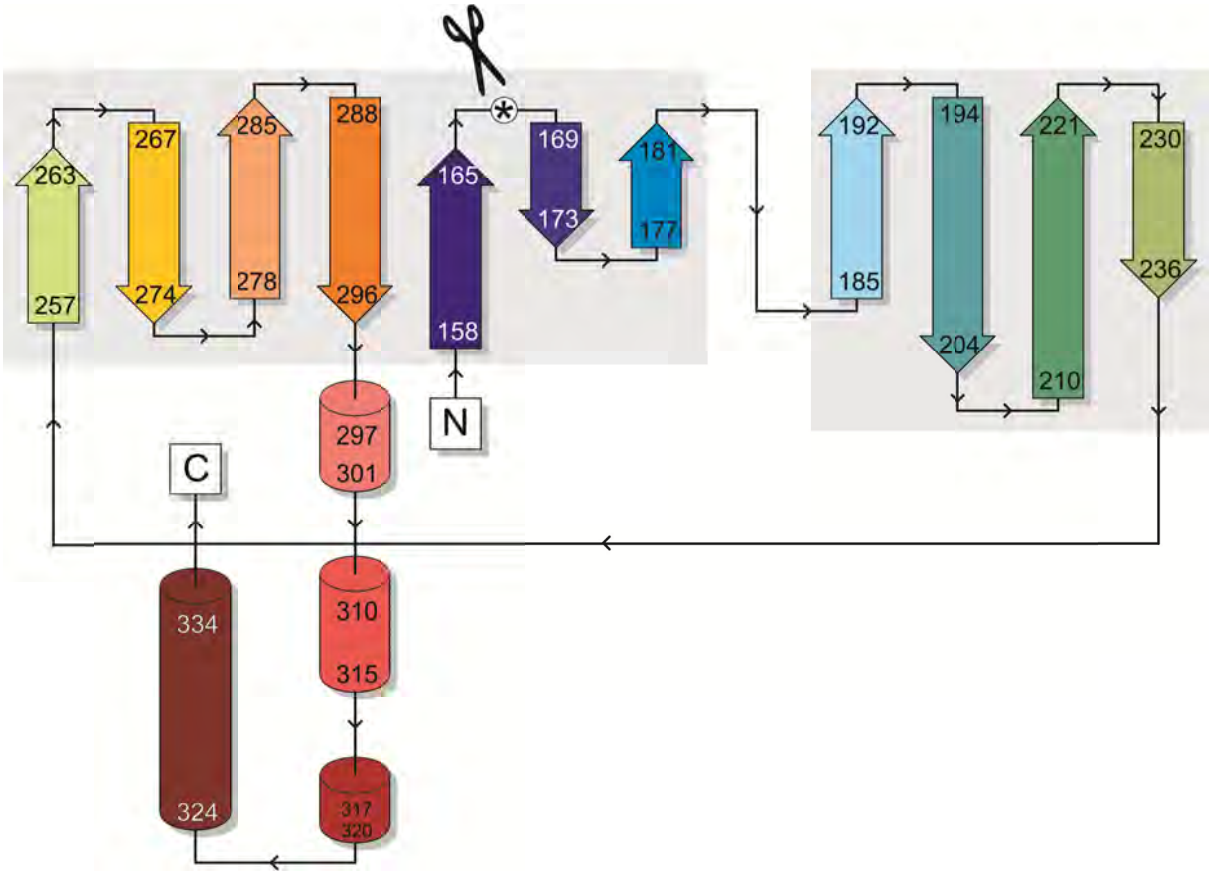

Fig. S2: Topology diagram of the RGMB structure. Colouring is as in Fig. **1**B. The autocatalytic cleavage site is highlighted by an asterisk. The figure is adapted from PDBSUM (http://www.ebi.ac.uk/pdbsum/). RGMs comprise a novel protein fold consisting of a tightly packed β-sandwich with seven strands on one sheet and four strands on the other.

A

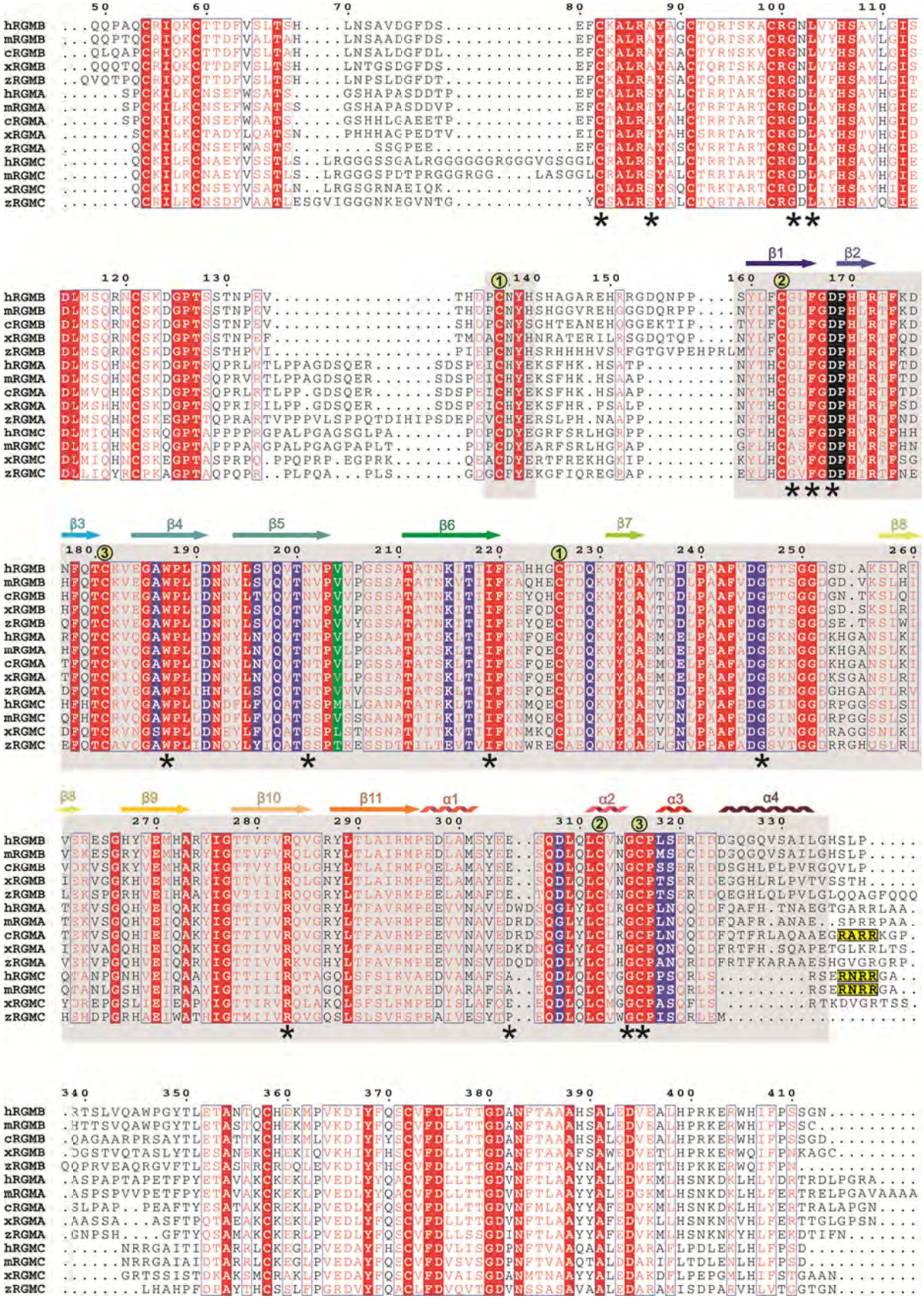
hRGMB
mRGMB
cRGMB
xRGMB
zRGMB
hRGMA
mRGMA
cRGMA
xRGMA
zRGMA
hRGMC
mRGMC
xRGMC
zRGMC
β1
β2
β3
β4
β5
β6
β7
β8
β9
β10
β11
α1
α2
α3
α4

B

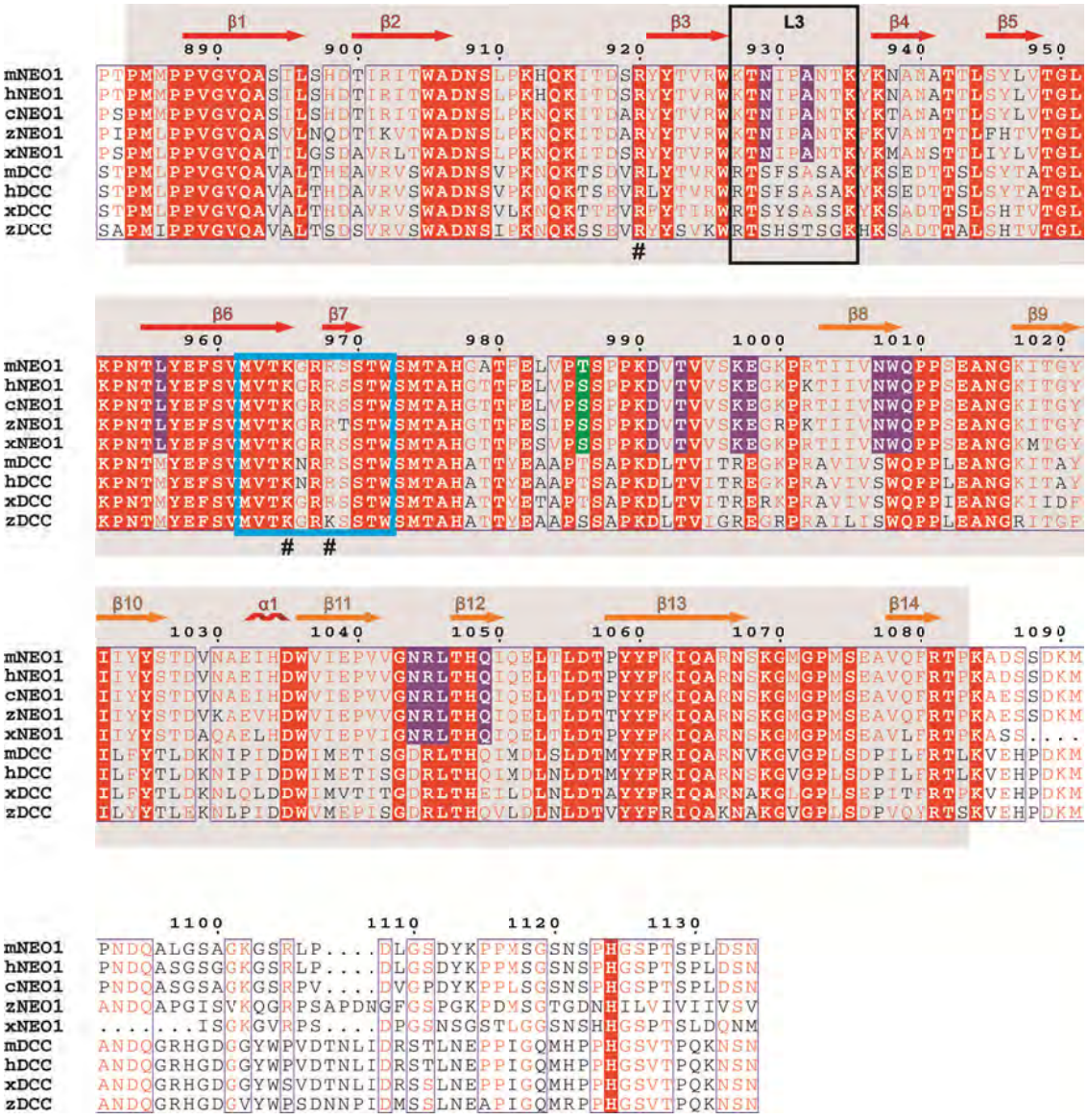

Fig. S3: Sequence alignments of the vertebrate RGM (A) and NEO1/DCC (B) family members. Sequences were aligned using MULTALIN (bioinfo.genotoul.fr/multalin/multalin.html) and formatted with ESPRIPT (espript.ibcp.fr/ESPript/ESPript/). Numbering corresponds to the full length human RGMB (A) and mouse NEO1 (B) (including the secretion signal). Secondary structure assignments are displayed above the alignment and colour-coded as in Fig. 1B (for RGMs) and Fig. 1D (for NEO1), respectively. Residues contributing hydrophilic interactions to the RGMB-NEO1 complex are highlighted in blue (site-1) and green (site-2). Residues forming the RGM autocatalytic cleavage site are shown in black. The potential furin cleavage site in RGMs is highlighted as yellow box. Disease-related residues identified in human RGMC are marked below the sequences with an asterisk (*). Disulfide bridges are numbered in green. Hashtags mark the NEO1 residues interacting with SOS. The region of DCC identified to interact with glycosamino-glycans(53) and Netrin-1(54) is boxed in light blue. The grey box in the background indicates the amino acid residues present in the structure. All residues involved in the NEO1-RGMB site-1 and site-2 interactions are conserved amongst RGMs, suggesting that the site-1 and site-2 interfaces reveal a common architecture for RGM-NEO1 interactions (see also Fig. 2C and fig. S8C).

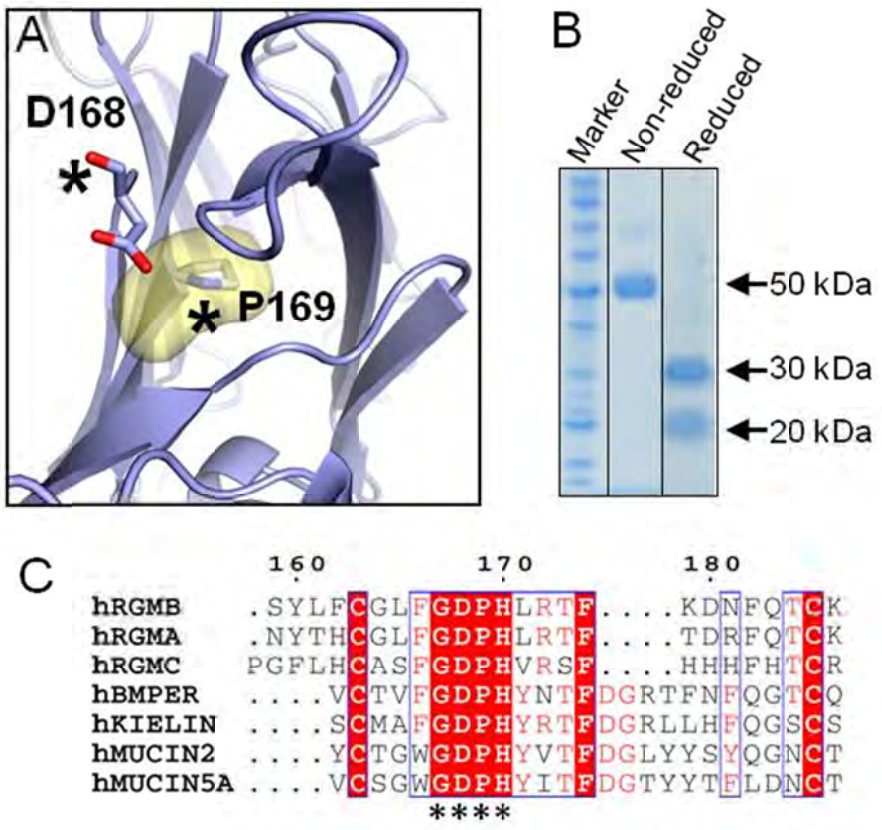

Fig. S4: The RGM autocatalytic cleavage site. (A) Close-up view of the RGMB autocatalytic cleavage site. Mechanistically, this involves intramolecular catalysis by aspartate carboxylate anion displacement of the protonated nitrogen of the peptide bond. Since the prolyl nitrogen has the strongest basicity of all amino acids, this enhances the peptide bond cleavage by increasing protonation of the leaving group which potentially occurs in lower pH environments (e.g. in the Golgi and secretory vesicles). The yellow sphere shows the solvent accessible surface of P169. **(B)** SDS-PAGE of SEC-purified human RGMA. All transiently expressed and secreted RGMA and RGMB proteins from human HEK293T cells are ~100% processed. **(C)** The RGM autocatalytic cleavage site ("GDPH") is conserved in various vWFD family members and has been functionally characterised in Mucins(*55*, *56*) and BMPER(*57*). However, RGM family members are missing the characteristic Gly-Leu-Cys-Gly motif towards the C-terminus of the domain(*29*), which makes it difficult to predict if the other vWfD family members adopt a similar fold like RGMs. The sequence alignment was generated as in figS3. Asterisks highlight the conserved autocleavage site residues. Human BMPER: Uniprot Q8N8U9, human Kielin: UniProt Q6ZWJ8, human Mucin 2: UniProt Q02817, human Mucin 5A: UniProt P98088.

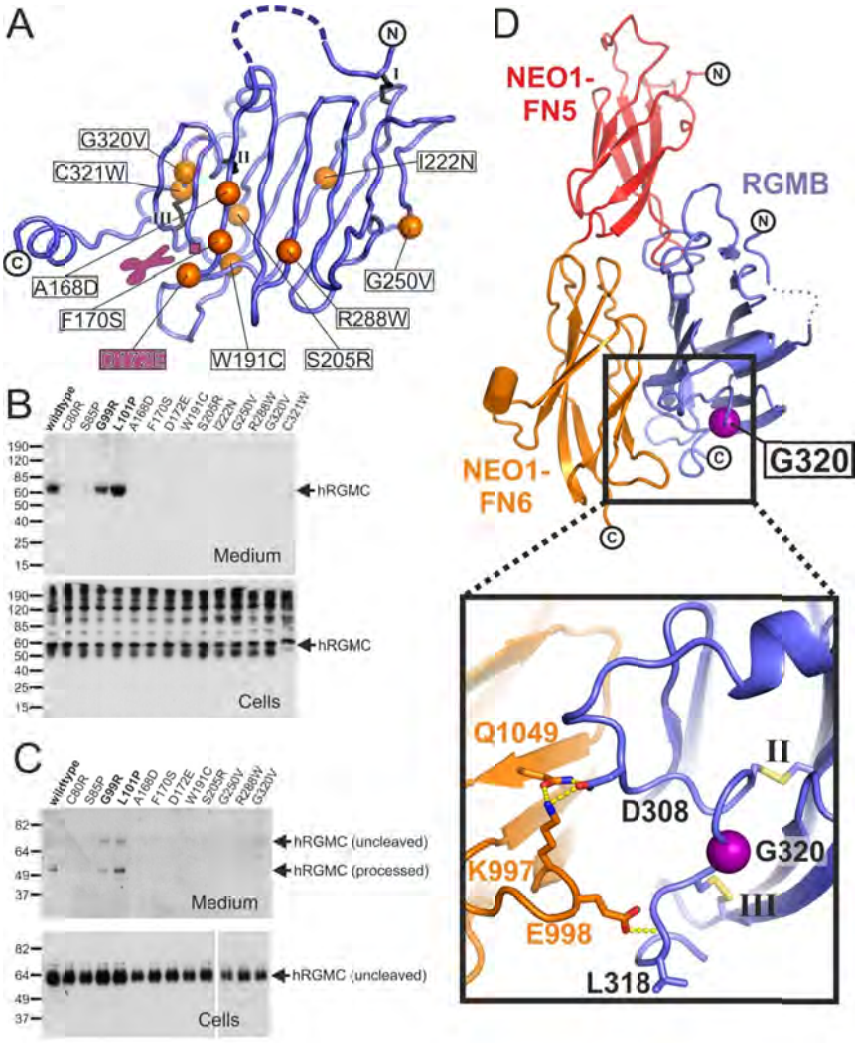

Fig. S5: Structural and functional characterisation of RGMC mutations causing juvenile hemachromatosis. (A) RGMC mutations mapped onto the RGMB structure. Ten of the reported mutations map onto the domain of RGM observed in the crystal structure. Equivalent residues on RGMB are shown as orange spheres. The autocatalytic cleavage site is highlighted. **(B-C)** Small scale expression test of the disease-related RGMC mutants. All mutants were generated in the $eRGMC_{AAA}$ background. Top panel: medium; lower panel: cells. Of the 14 mutants only two (G99R and L101P) were secreted at levels observed for the wildtype. G99R and L101P map to the N-terminal domain which is not present in the crystal structure. SDS-PAGE analysis was carried out under non-reducing (B) as well as reducing (C) conditions. Secreted human RGMC exists in a major, processed and a minor, uncleaved form, which is in contrast to secreted RGMA and RGMB proteins (fig S4). **(D)** The RGMC-G320V mutation. Colour coding is as in Fig. 1D. The Cα atom of G320 is shown as magenta sphere. Although all RGMC mutations that may impact onto the site-1 interface impair secretion in this study, the JHH-linked RGMC mutation $Gly320Val^{RGMC}$ has been successfully expressed in a secreted form in a stable expression system(59). The authors showed that this mutant protein failed to interact with NEO1. Intriguingly, Gly-320 (corresponding to Gly-315 in human RGMB) is located close to the site-1 interface. A mutation of G320 to valine can potentially cause a rearrangement of RGM disulphide bridges II and III, as well as impair the site-1 NEO1-RGM interface including RGMB residues D308 and L318, which form hydrogen bonds with NEO1 residues K997, E998 and Q1049.

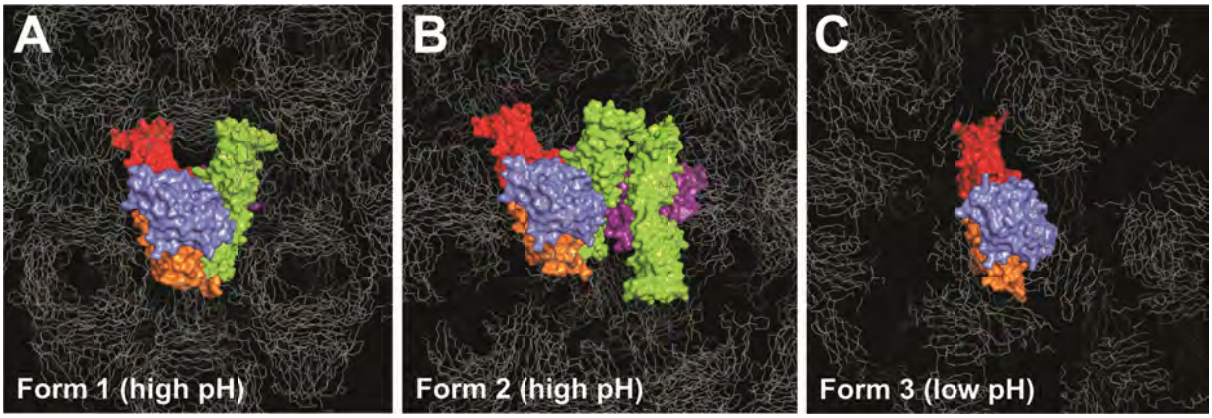

Fig. S6: Crystal packing of the different RGMB-NEO1 complex structures. (A) eRGMB-NEO1$_{FN56}$ Form 1, **(B)** eRGMB-NEO1$_{FN56}$ Form 2 and **(C)** eRGMB-NEO1$_{FN56}$ Form 3. Orientation and colour coding is as in Fig. 1D, right panel. The neutral pH crystal form 1 contains the 2:2 complex in the asymmetric unit. In form 2 the 2:2 complex is built by a two-fold crystallographic axis. The low pH crystal form 3 contains only the 1:1 complex in the asymmetric unit. For crystallographic details see table S1.

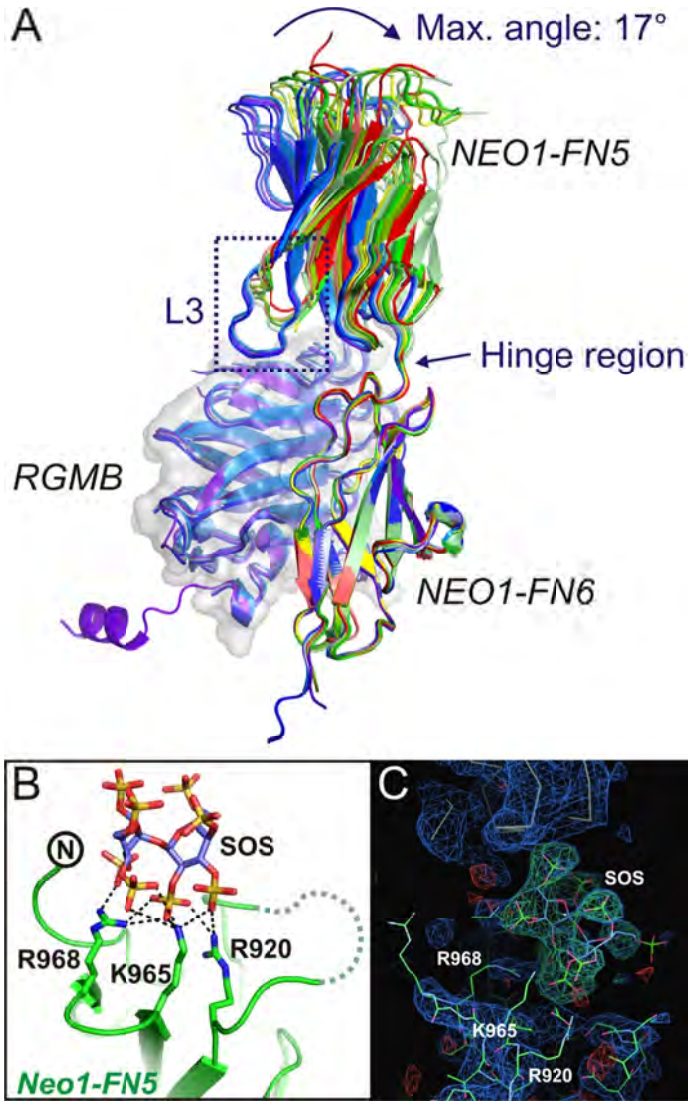

Fig. S7: NEO1 structure comparison of apo and complex-bound forms. (A) Superpositions calculated based on the NEO1-FN6 domain. $NEO1_{FN56}$ Form 1 (4 molecules, coloured in different green shades), $NEO1_{FN56}$ Form 2 (2 molecules, coloured in different cyan shades), $NEO1_{FN56}$-sucrose octasulphate (SOS) (2 molecules, coloured in different red shades), $NEO1_{FN56}$ previously reported(39) (PDB Id 3P4L, 1 molecule, coloured in yellow) eRGMB-$NEO1_{FN56}$ Form 1 (2 molecules NEO1 and RGMB coloured in dark blue), eRGMB-$NEO1_{FN56}$ Form 2 (2 molecules NEO1 and RGMB, coloured in light blue), eRGMB-$NEO1_{FN56}$ Form 3 (1 molecule NEO1 and RGMB, coloured in light violet). Superpositions of all 5 site-1 complex molecules result in a very good overall overlay, whereas the NEO1 apo structures show significant flexibility between the relative orientation of the FN5 and FN6 domains. The L3 loop, which forms the major interaction site of NEO1-FN5 with RGMB is flexible or disordered in the NEO1 apo structures, suggesting that RGMB adds rigidity towards the conformation of the NEO1 FN5-FN6 interface. **(B)** Close-up of the NEO1-SOS binding site. The SOS molecule sits on top of the NEO1-FN5 domain. Interactions of the SOS sulphate groups involve the positively charged side chains of arginines 920 and 968 and lysine 965 (see also fig. S3B). It is worth noting that the equivalent residues 965 and 968 in DCC have been previously implicated in glycosamino-glycan(53) and Netrin-1 binding(54). **(C)** SigmaA-weighted $2F_O$-F_C map (blue, 1.0 σ) and F_O-F_C map (green/red, ±3.0 σ) from PHENIX(42) after rigid body and positional refinement calculated without the SOS molecule.

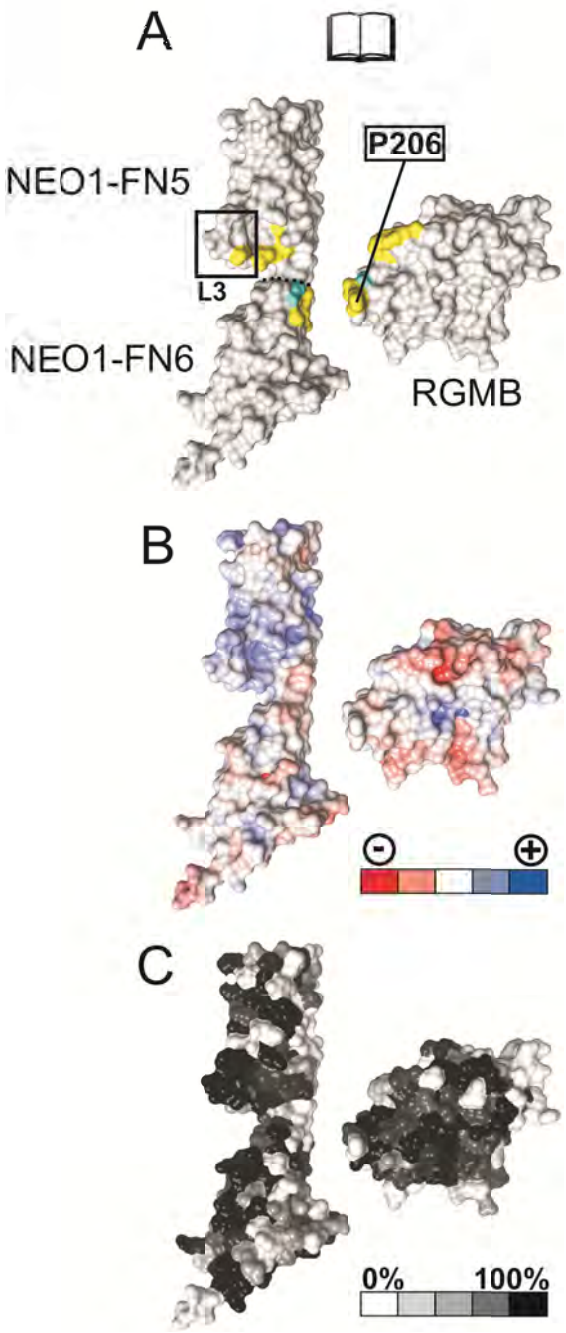

Fig. S8. The RGMB-NEO1 site-2 interactions. The eRGMB-NEO1$_{FN56}$ complex is shown in surface representation in an open book view. **(A)** Interface residues are highlighted (non-bonded interactions: yellow; hydrophilic interactions: cyan). The RGMB L3 loop is marked. In total the site-2 interface is composed of 1 hydrogen bond and 25 non-bonded contacts (see also Fig. 2D). **(B)** Electrostatic potential from red (-8 kbT/ec) to blue (+8 kbT/ec). The majority of the interactions are formed by hydrophobic residues. **(C)** The complex is colour-coded according to residue conservation (from non-conserved, white, to conserved, black) based on alignments containing sequences from 17 NEO1 orthologues and 94 RGM orthologues and paralogues from vertebrates.

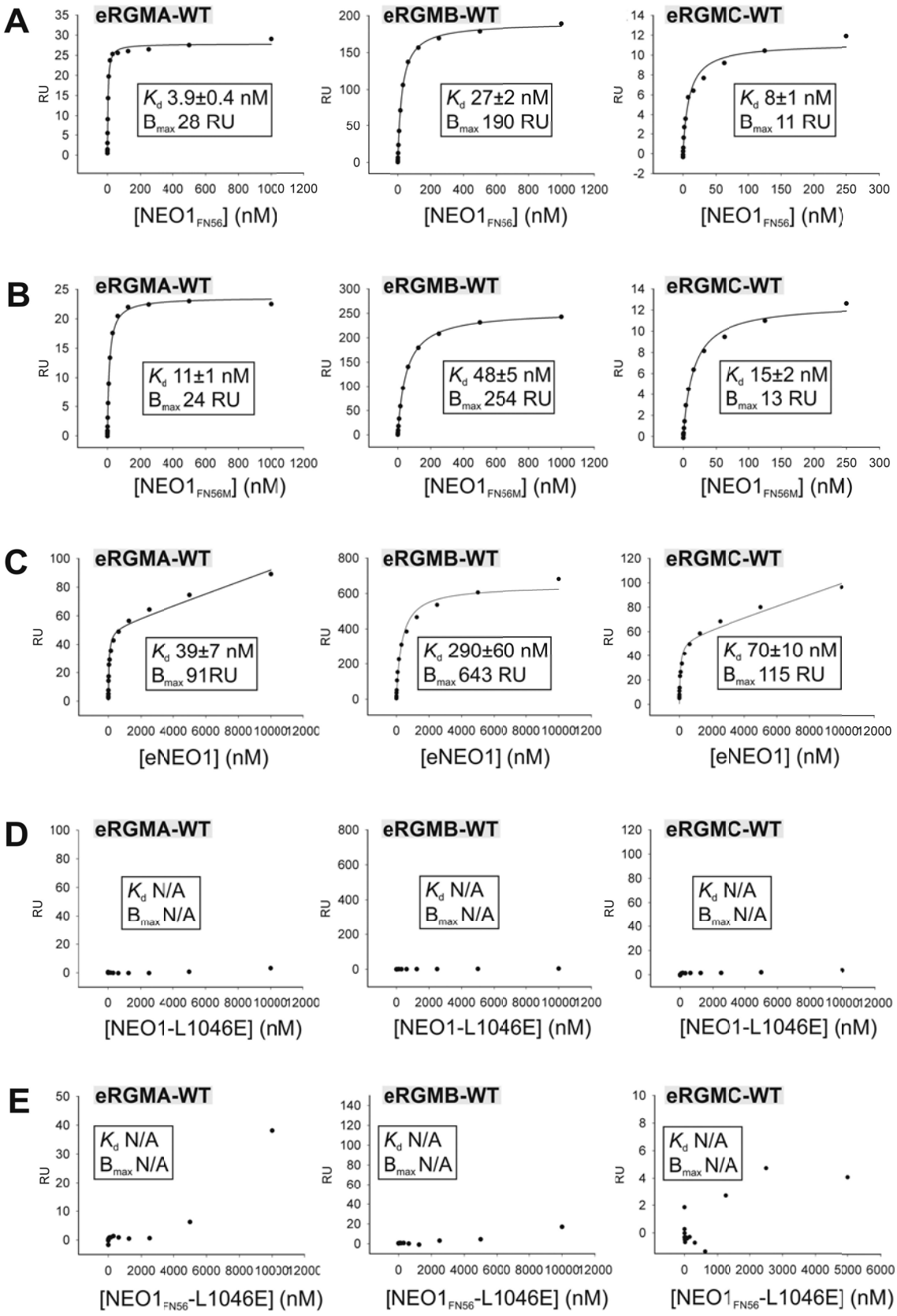
A
eRGMA-WT
K_d 3.9±0.4 nM
B_{max} 28 RU
RU
[NEO1$_{FN56}$] (nM)
eRGMB-WT
K_d 27±2 nM
B_{max} 190 RU
RU
[NEO1$_{FN56}$] (nM)
eRGMC-WT
K_d 8±1 nM
B_{max} 11 RU
RU
[NEO1$_{FN56}$] (nM)
B
eRGMA-WT
K_d 11±1 nM
B_{max} 24 RU
RU
[NEO1$_{FN56M}$] (nM)
eRGMB-WT
K_d 48±5 nM
B_{max} 254 RU
RU
[NEO1$_{FN56M}$] (nM)
eRGMC-WT
K_d 15±2 nM
B_{max} 13 RU
RU
[NEO1$_{FN56M}$] (nM)
C
eRGMA-WT
K_d 39±7 nM
B_{max} 91RU
RU
[eNEO1] (nM)
eRGMB-WT
K_d 290±60 nM
B_{max} 643 RU
RU
[eNEO1] (nM)
eRGMC-WT
K_d 70±10 nM
B_{max} 115 RU
RU
[eNEO1] (nM)
D
eRGMA-WT
K_d N/A
B_{max} N/A
RU
[NEO1-L1046E] (nM)
eRGMB-WT
K_d N/A
B_{max} N/A
RU
[NEO1-L1046E] (nM)
eRGMC-WT
K_d N/A
B_{max} N/A
RU
[NEO1-L1046E] (nM)
E
eRGMA-WT
K_d N/A
B_{max} N/A
RU
[NEO1$_{FN56}$-L1046E] (nM)
eRGMB-WT
K_d N/A
B_{max} N/A
RU
[NEO1$_{FN56}$-L1046E] (nM)
eRGMC-WT
K_d N/A
B_{max} N/A
RU
[NEO1$_{FN56}$-L1046E] (nM)

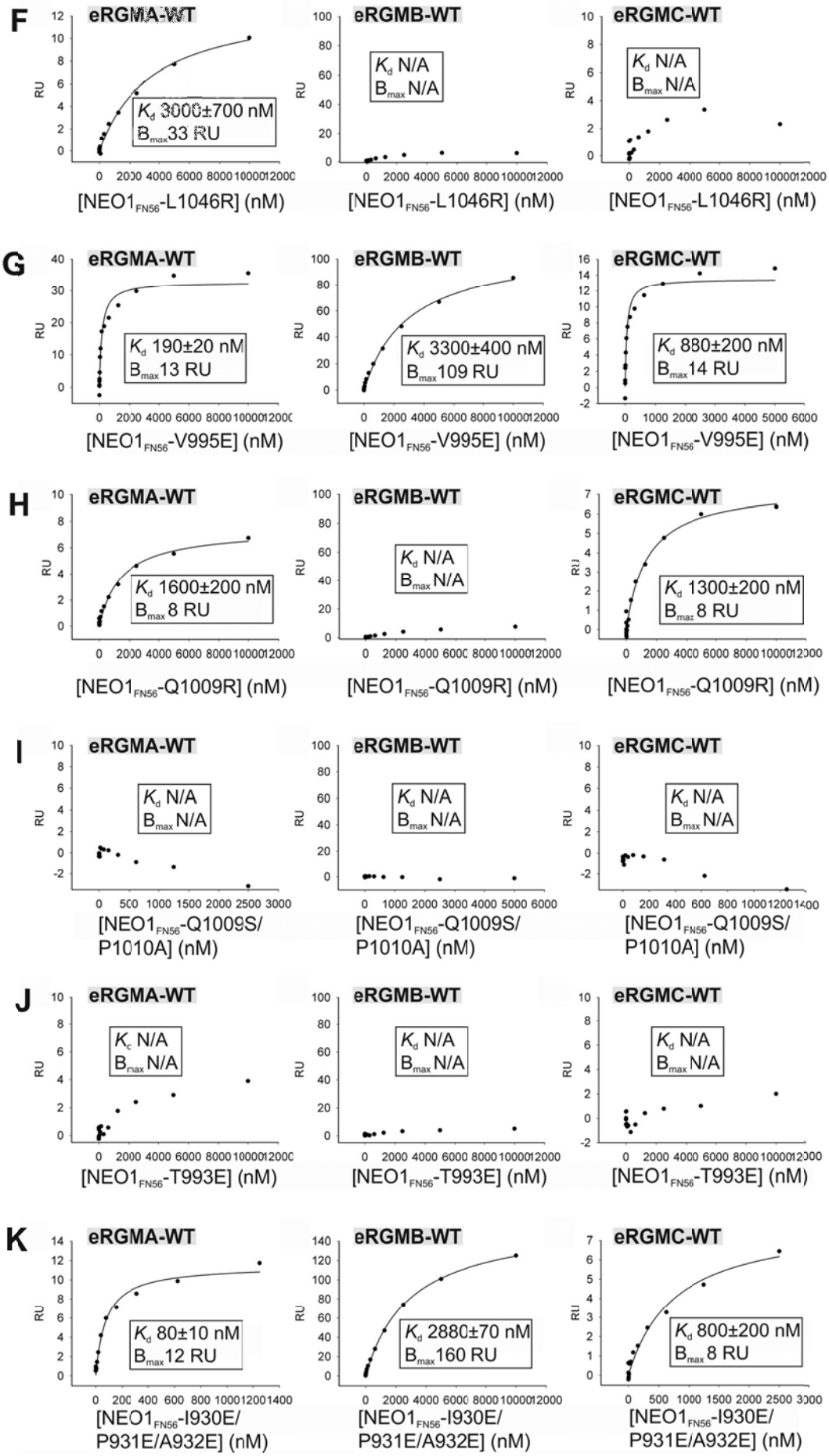
F
eRGMA-WT
K_d 3000±700 nM
B_{max} 33 RU
[NEO1$_{FN56}$-L1046R] (nM)
eRGMB-WT
K_d N/A
B_{max} N/A
[NEO1$_{FN56}$-L1046R] (nM)
eRGMC-WT
K_d N/A
B_{max} N/A
[NEO1$_{FN56}$-L1046R] (nM)
G
eRGMA-WT
K_d 190±20 nM
B_{max} 13 RU
[NEO1$_{FN56}$-V995E] (nM)
eRGMB-WT
K_d 3300±400 nM
B_{max} 109 RU
[NEO1$_{FN56}$-V995E] (nM)
eRGMC-WT
K_d 880±200 nM
B_{max} 14 RU
[NEO1$_{FN56}$-V995E] (nM)
H
eRGMA-WT
K_d 1600±200 nM
B_{max} 8 RU
[NEO1$_{FN56}$-Q1009R] (nM)
eRGMB-WT
K_d N/A
B_{max} N/A
[NEO1$_{FN56}$-Q1009R] (nM)
eRGMC-WT
K_d 1300±200 nM
B_{max} 8 RU
[NEO1$_{FN56}$-Q1009R] (nM)
I
eRGMA-WT
K_d N/A
B_{max} N/A
[NEO1$_{FN56}$-Q1009S/ P1010A] (nM)
eRGMB-WT
K_d N/A
B_{max} N/A
[NEO1$_{FN56}$-Q1009S/ P1010A] (nM)
eRGMC-WT
K_d N/A
B_{max} N/A
[NEO1$_{FN56}$-Q1009S/ P1010A] (nM)
J
eRGMA-WT
K_c N/A
B_{max} N/A
[NEO1$_{FN56}$-T993E] (nM)
eRGMB-WT
K_d N/A
B_{max} N/A
[NEO1$_{FN56}$-T993E] (nM)
eRGMC-WT
K_d N/A
B_{max} N/A
[NEO1$_{FN56}$-T993E] (nM)
K
eRGMA-WT
K_d 80±10 nM
B_{max} 12 RU
[NEO1$_{FN56}$-I930E/ P931E/A932E] (nM)
eRGMB-WT
K_d 2880±70 nM
B_{max} 160 RU
[NEO1$_{FN56}$-I930E/ P931E/A932E] (nM)
eRGMC-WT
K_d 800±200 nM
B_{max} 8 RU
[NEO1$_{FN56}$-I930E/ P931E/A932E] (nM)

Fig. S9: SPR data of NEO1-RGM interactions. Binding of NEO1 constructs and mutants to the full-length ectodomains of RGMA (left panel), RGMB (middle panel) and RGMC (right panel), respectively. Graphs show a plot of the equilibrium binding response (response units (RU)) against concentration of the used NEO1 constructs. All experiments were performed in duplicate. Best-fit binding curves calculated using a 1:1 binding model are shown as lines. If not differently stated in the graph, the chip concentrations were 80 RU, 500 RU and 90 RU for eRGMA, eRGMB and eRGMC, respectively. Corresponding ligands (immobilised on the chip) are indicated in grey boxes. Binding constants (K_d) are given as mean with the error representing the standard error of the mean. N/A: not applicable. NEO1 constructs comprising only the FN5 and FN6 domains ($NEO1_{FN56}$ and $NEO1_{FN56M}$) (Fig. 7A and B) showed even tighter binding to all RGMs compared to the full-length NEO1 ectodomain (Fig. 7C), possibly explained by better accessibility of the RGMs to the truncated constructs.

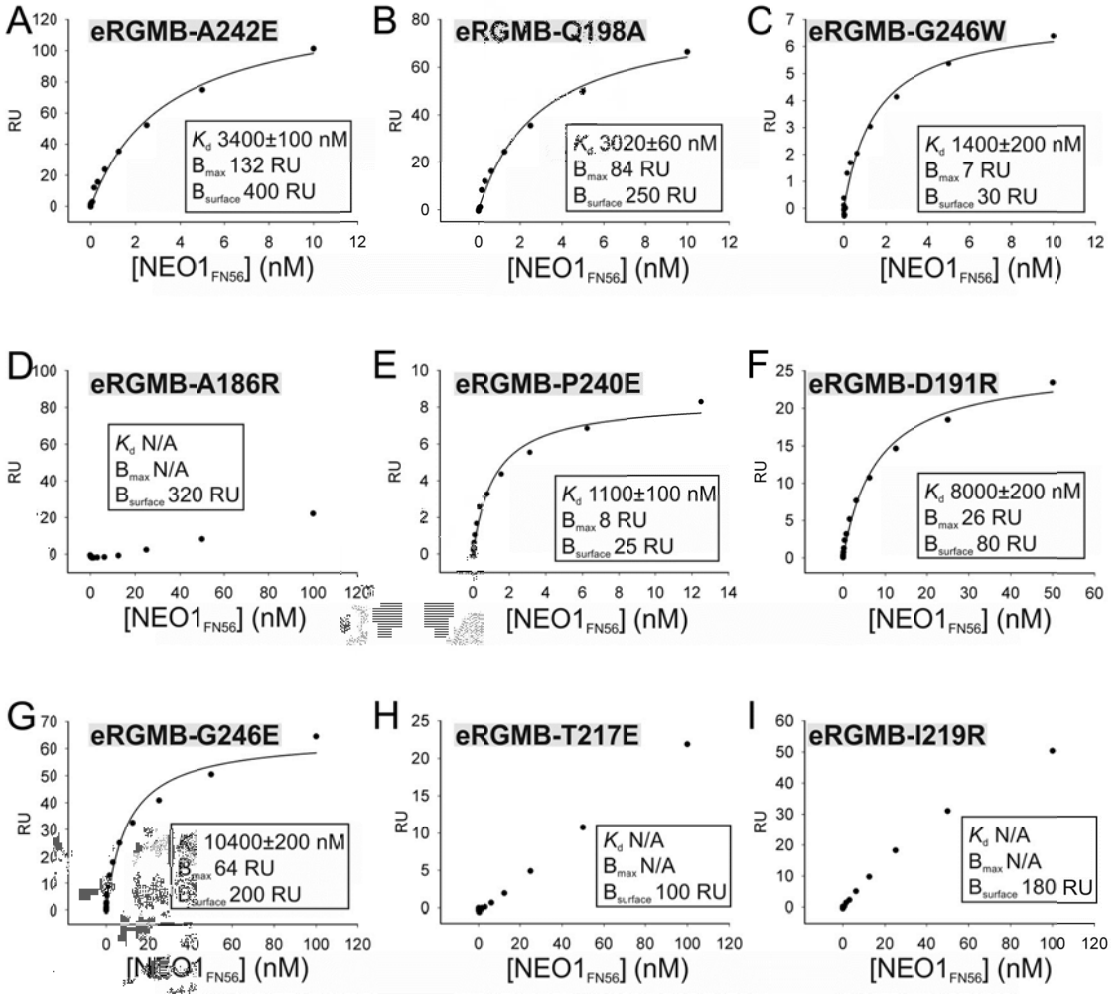

Fig. S10: Binding of NEO1 to different RGMB mutants. Graphs show a plot of the equilibrium binding response (response units (RU)) against $NEO1_{FN56}$ concentration ranging from 6 nM to 100 nM. All experiments were performed in duplicate. Best-fit binding curves were calculated using a 1:1 binding model shown as lines. The chip concentrations of the RGMB constructs immobilised on the chip are given as $B_{surface}$. Binding constants (K_d) are given as mean with the error representing the standard error of the mean. N/A: not applicable.

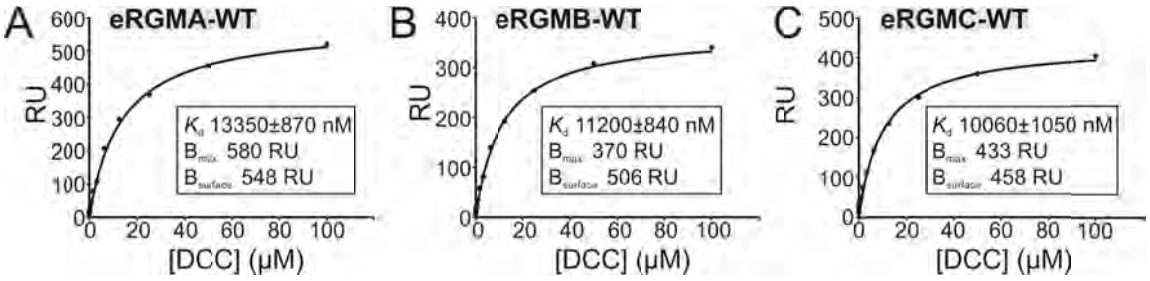

Fig. S11: Binding of DCC to RGMA (A), RGMB (B) and RGMC (C). Graphs show a plot of the equilibrium binding response (response units (RU)) against the concentration of the full-length ectodomain of DCC ranging from 6 nM to 100 µM. All experiments were performed in duplicate. Best-fit binding curves were calculated using a 1:1 binding model shown as lines. The chip concentrations of the RGM constructs immobilised on the chip are given as $B_{surface}$. Binding constants (K_d) are given as mean with the error representing the standard error of the mean.

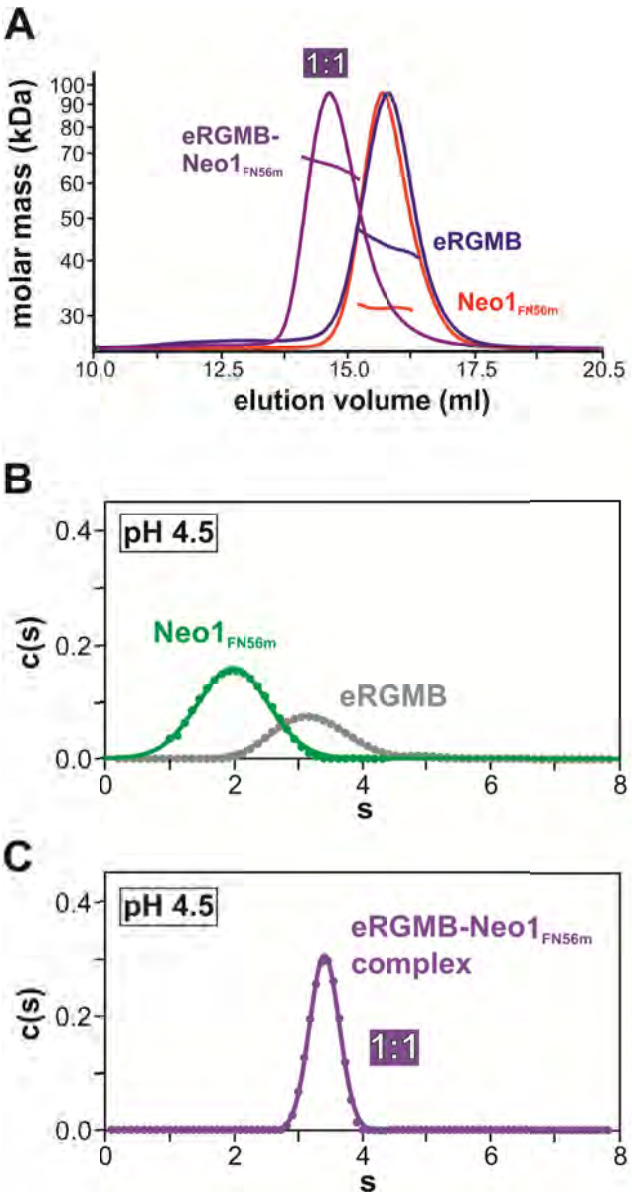

Fig. S12: Oligomeric behaviour of the RGMB-NEO1 complex. (A) Multi-angle light scattering (MALS) analysis of the RGMB-NEO1 complex. eRGMB (blue) and $NEO1_{FN56M}$ (red) behave as monomers with the following molecular weights (measured/theoretical): eRGMB: 42.64±0.1/43.35 kDa; $NEO1_{FN56M}$: 31.04±0.1/31.05 kDa. The eRGMB-$NEO1_{FN56M}$ complex (magenta) behaves as a heterodimeric (one RGMB and one NEO1) complex (molecular weight measured/theoretical: 69.04±0.1/74.40 kDa) at concentrations up to 3 µM. Theoretical molecular weights of glycosylated proteins were calculated using PROTPARAM at the EXPASY server (www.expasy.ch). **(B-C)** Analytical ultracentrifugation sedimentation velocity experiments of (B) eRGMB (grey) and $NEO1_{FN56M}$ (green) and (C) the eRGMB-$NEO1_{FN56M}$ complex at pH 4.5. Distribution plots obtained from the fitting of SV data using a continuous *c(s)* distribution model (solid line Gaussian fit to data plotted as symbols) are shown (compare to Fig. 3C-E). Individual Gaussian peaks contributing to the overall distributions are displayed in dotted lines for the eRGMB (B, RMSD: 0.0016), $NEO1_{FN56M}$ (B, RMSD: 0.0023) and the eRGMB-NEO1 (F, RMSD: 0.0027) complexes. The individual components run as discrete single, likely monomeric species. The eRGMB-$NEO1_{FN56M}$ complex shows a single species likely corresponding to the 1:1 complex.

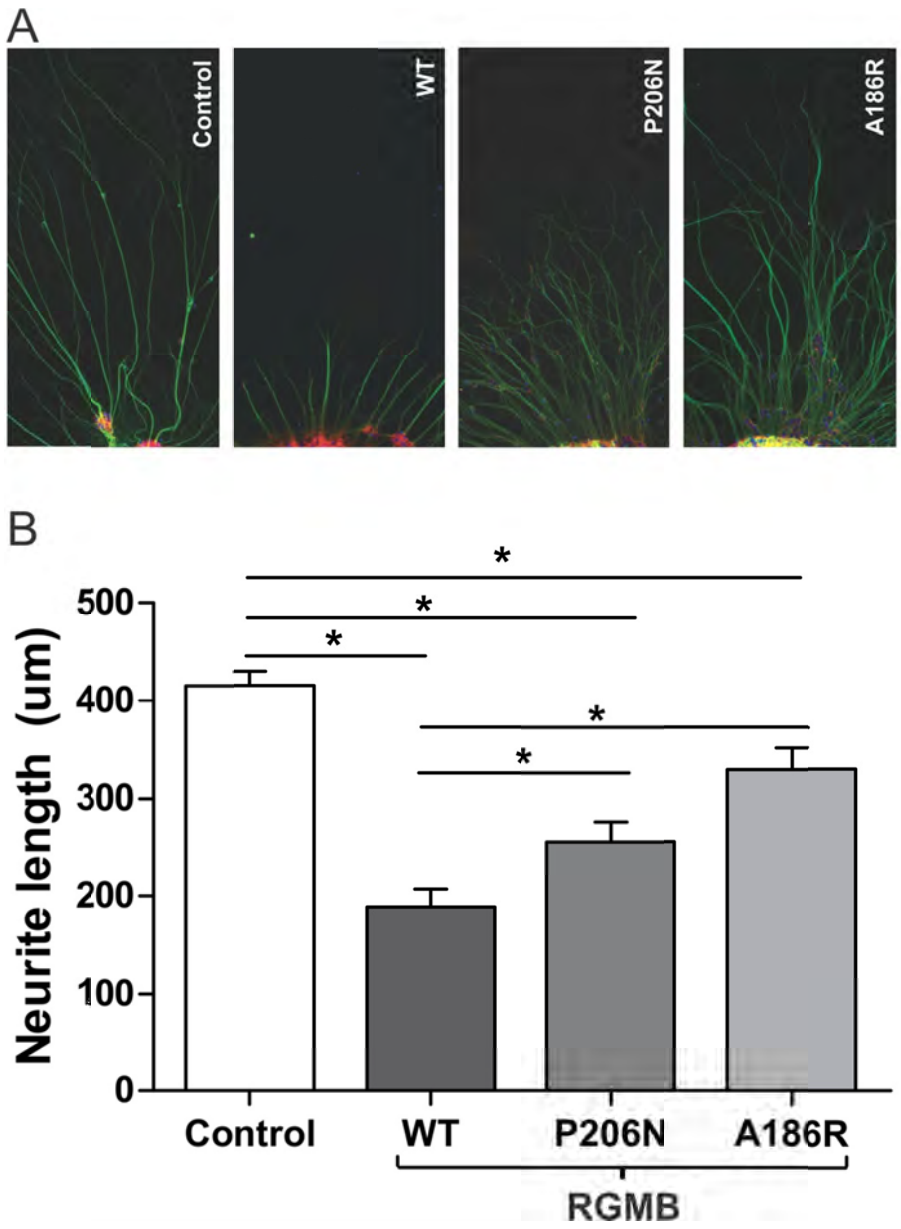

Fig. S13: Functional analysis of the effects of RGMB site 1 and 2 mutations on neurite growth. **(A)** Higher magnification of representative neuronal explants used for the quantification of neurite length shown in Fig. 4. The length of individual, non-fasciculated neurites was determined by measuring the distance between the edge of the explant and the growth cone of >20 neurites per explant. **(B)** Average neurite length per explant was calculated for each condition (three independent experiments, total number of explants analyzed per condition; WT n=27, P206N n=24, A186R n=26, control n=23), error bars are SEM, * $P<0.05$.

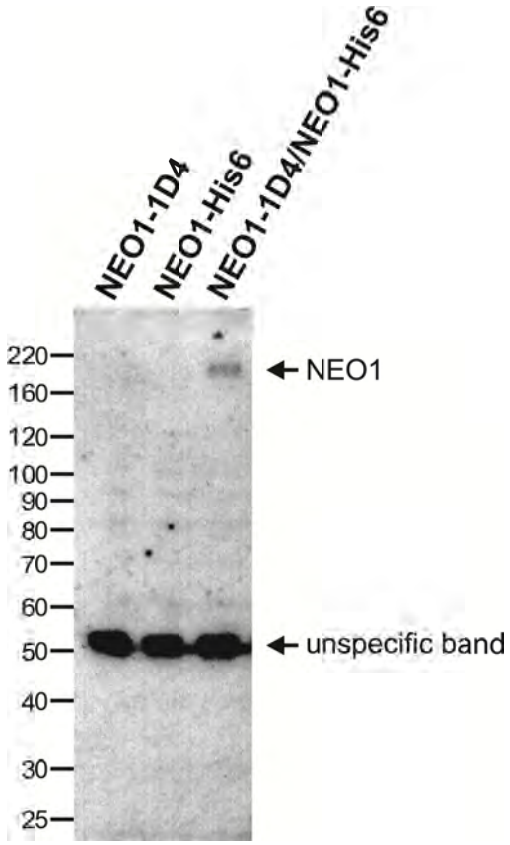

Fig. S14: Pre-formed NEO1 dimers can be isolated from the cell membrane. Full-length NEO1-1D4 and NEO1-His6 proteins were extracted from the membranes of co-transfected cells. Proteins were solubilised in detergent-containing buffer and NEO1-1D4 proteins were immobilised on 1D4-antibody-conjugated sepharose beads. The beads were washed several times and the bound protein complexes were eluted from the beads by competition with high concentrations of 1D4 peptide. The eluted protein complexes were separated by SDS-PAGE (4-12 % Bis Tris gradient gel), and analysed by Western blotting with a mouse anti-His6 antibody probe. NEO1-1D4 was shown to pull-down NEO1-His6 suggesting NEO1 dimers form in the membrane. Non-specific binding of NEO1-His6 to the 1D4-antibdy-conjugated sepharose beads was not observed. Non-specific binding of the mouse anti-His6 antibody to NEO1-1D4 was also not observed.

Table S1. Crystallographic data collection and refinement statistics

	$NEO1_{FN56}$-eRGMB Form 1 (high pH)	**$NEO1_{FN56}$-eRGMB Form 2 (high pH)**	**$NEO1_{FN56}$-eRGMB Form 3 (low pH)**	**$NEO1_{FN56}$ Form 1**	**$NEO1_{FN56}$ Form 2**	**$NEO1_{FN56}$-SOS**
DATA COLLECTION						
X-ray source	DIAMOND-I03	DIAMOND-I03	DIAMOND-I03	ESRF-ID14-EH4	DIAMOND-I03	ESRF-ID14-EH4
Resolution	30.0-2.3 (2.4-2.3)	50.0-6.6 (6.8-6.6)	50.0-2.8 (2.9-2.8)	30.0-2.9 (3.0-2.9)	30.0-2.7 (2.8-2.7)	30.0- 3.2 (3.3-3.2)
Space group	$P2_12_12_1$	$P3_212$	$P4_12_12$	$P3_121$	$P2_1$	$C222_1$
Cell dimensions [Å]	a= 91.3 Å b = 100.4 Å c = 103.7 Å	a= 109.7 Å b = 109.7 Å c = 187.9 Å	a = 116.9 b = 116.9 c = 91.8	a = 103.6 Å b = 103.6 Å c = 110.8 Å	a = 59.0 Å b = 97.4 Å c = 91.3 Å β = 106.4°	a = 96.2 Å b = 157.8 Å c = 89.9 Å
Solvent content [%] (mols per AU)	55 (2 mols eRGMB, 2 mols $NEO1_{FN56}$)	65 (2 mols eRGMB, 2 mols $NEO1_{FN56}$)	68 (1 mol eRGMB, 1 mol $NEO1_{FN56}$)	68 (2 mols $NEO1_{FN56}$)	56 (4 mols $NEO1_{FN56}$)	69 (2 mols $NEO1_{FN56}$)
Wilson B factor [$Å^2$]	57	182	84	64	81	67
Unique reflections	42796 (2990)	2508 (181)	16223 (1167)	15545 (1531)	26660 (2518)	11572 (820)
Completeness [%]	99.3 (95.6)	97.7 (97.4)	99.9 (99.4)	99.9 (100.0)	97.7 (92.7)	99.4 (98.6)
R_{merge} [%][a]	9.2 (84.1)	23.3 (78.9)	8.9 (90.8)	13.5 (86.8)	8.0 (82.9)	11.4 (83.0)
I/σI	10.2 (1.3)	7.5 (2.3)	15.5 (1.9)	10.8 (1.5)	11.3 (1.2)	16.3 (2.9)
Redundancy	6.0 (4.0)	6.0 (5.0)	8.4 (7.8)	4.2 (4.3)	2.3 (2.2)	10.0 (10.3)
REFINEMENT						
Resolution range [Å]	30.0-2.3 (2.36-2.30)	50.0-6.6 (8.3-6.6)	50.0-2.8 (3.0-2.8)	30.0-2.9 (3.1-2.9)	30.0-2.7 (2.8-2.7)	30.0- 3.2 (3.5-3.2)
Number of reflections	42757 (2852)	2488 (1116)	16180 (2854)	15443 (2737)	26625 (2837)	11548 (2686)
No. of atoms (protein/NAG/SOS/H_2O)	5771/28/0/329	5750/0/0/0	2905/14/0/0	3106/28/0/0	6277/56/0/0	2951/14/110/0
B factors [$Å^2$] (protein/NAG/SOS/H_2O)	52/80/0/48	-	76/119/0/0	69/110/0/0	89/109/0/0	98/109/180/0
R_{factor} [%)][c]	22.1 (21.0)	26.1 (28.9)	18.7 (21.9)	20.6 (27.2)	20.1 (24.5)	22.0 (24.2)
R_{free} [%] [d]	26.6 (23.1)	27.2 (29.3)	20.3 (26.8)	23.2 (31.7)	22.4 (25.6)	26.5 (28.0)
r.m.s.d. bonds [Å]	0.010	0.019	0.009	0.010	0.010	0.010
r.m.s.d. angles [deg]	1.21	1.90	1.18	1.21	1.13	1.19
Ramachandran statistics						
Favoured [%]	94.6	94.0	96.1	96.6	97.6	95.9
Disallowed [%]	0	0.7	0	0	0	0

r.m.s.d.: root mean square deviation from ideal geometry. Numbers in parentheses refer to the appropriate outer shell.

[a] $R_{merge} = \Sigma_{hkl} \Sigma_i |I(hkl;i) - \langle I(hkl) \rangle| / \Sigma_{hkl} \Sigma_i I(hkl;i)$, where $I(hkl;i)$ is the intensity of an individual measurement and $\langle I(hkl) \rangle$ is the average intensity from multiple observations.

[b] $R_{factor} = \Sigma_{hkl} ||F_{obs}| - k|F_{calc}|| / \Sigma_{hkl} |F_{obs}|$.

[c] R_{free} equals the *R*-factor against 5% of the data removed prior to refinement.

References and Notes

1. P. P. Monnier *et al*., RGM is a repulsive guidance molecule for retinal axons. *Nature* **419**, 392 (2002). doi:10.1038/nature01041 Medline

2. V. Niederkofler, R. Salie, M. Sigrist, S. Arber, Repulsive guidance molecule (RGM) gene function is required for neural tube closure but not retinal topography in the mouse visual system. *J. Neurosci.* **24**, 808 (2004). doi:10.1523/JNEUROSCI.4610-03.2004 Medline

3. V. Mirakaj *et al*., Repulsive guidance molecule-A (RGM-A) inhibits leukocyte migration and mitigates inflammation. *Proc. Natl. Acad. Sci. U.S.A.* **108**, 6555 (2011). doi:10.1073/pnas.1015605108 Medline

4. Y. Xia *et al*., Dragon (repulsive guidance molecule b) inhibits IL-6 expression in macrophages. *J. Immunol.* **186**, 1369 (2011). doi:10.4049/jimmunol.1002047 Medline

5. G. Papanikolaou *et al*., Mutations in HFE2 cause iron overload in chromosome 1q-linked juvenile hemochromatosis. *Nat. Genet.* **36**, 77 (2004). doi:10.1038/ng1274 Medline

6. R. Muramatsu *et al*., RGMa modulates T cell responses and is involved in autoimmune encephalomyelitis. *Nat. Med.* **17**, 488 (2011). doi:10.1038/nm.2321 Medline

7. V. S. Li *et al*., Frequent inactivation of axon guidance molecule RGMA in human colon cancer through genetic and epigenetic mechanisms. *Gastroenterology* **137**, 176 (2009). doi:10.1053/j.gastro.2009.03.005 Medline

8. S. Rajagopalan *et al*., Neogenin mediates the action of repulsive guidance molecule. *Nat. Cell Biol.* **6**, 756 (2004). doi:10.1038/ncb1156 Medline

9. S. Conrad, H. Genth, F. Hofmann, I. Just, T. Skutella, Neogenin-RGMa signaling at the growth cone is bone morphogenetic protein-independent and involves RhoA, ROCK, and PKC. *J. Biol. Chem.* **282**, 16423 (2007). doi:10.1074/jbc.M610901200 Medline

10. K. Hata *et al*., RGMa inhibition promotes axonal growth and recovery after spinal cord injury. *J. Cell Biol.* **173**, 47 (2006). doi:10.1083/jcb.200508143 Medline

11. J. L. Babitt *et al*., Bone morphogenetic protein signaling by hemojuvelin regulates hepcidin expression. *Nat. Genet.* **38**, 531 (2006). doi:10.1038/ng1777 Medline

12. Z. Zhou *et al*., Neogenin regulation of BMP-induced canonical Smad signaling and endochondral bone formation. *Dev. Cell* **19**, 90 (2010). doi:10.1016/j.devcel.2010.06.016 Medline

13. D. H. Lee *et al*., Neogenin inhibits HJV secretion and regulates BMP-induced hepcidin expression and iron homeostasis. *Blood* **115**, 3136 (2010). doi:10.1182/blood-2009-11-251199 Medline

14. A. S. Zhang *et al*., Evidence that inhibition of hemojuvelin shedding in response to iron is mediated through neogenin. *J. Biol. Chem.* **282**, 12547 (2007). doi:10.1074/jbc.M608788200 Medline

15. J. P. Xiong *et al*., Crystal structure of the extracellular segment of integrin alpha Vbeta3 in complex with an Arg-Gly-Asp ligand. *Science* **296**, 151 (2002). doi:10.1126/science.1069040 Medline

16. M. E. Lidell, M. E. Johansson, G. C. Hansson, An autocatalytic cleavage in the C terminus of the human MUC2 mucin occurs at the low pH of the late secretory pathway. *J. Biol. Chem.* **278**, 13944 (2003). doi:10.1074/jbc.M210069200 Medline

17. N. H. Wilson, B. Key, Neogenin: one receptor, many functions. *Int. J. Biochem. Cell Biol.* **39**, 874 (2007). doi:10.1016/j.biocel.2006.10.023 Medline

18. K. Lai Wing Sun, J. P. Correia, T. E. Kennedy, Netrins: versatile extracellular cues with diverse functions. *Development* **138**, 2153 (2011). doi:10.1242/dev.044529 Medline

19. E. Stein, Y. Zou, M. Poo, M. Tessier-Lavigne, Binding of DCC by netrin-1 to mediate axon guidance independent of adenosine A2B receptor activation. *Science* **291**, 1976 (2001). doi:10.1126/science.1059391 Medline

20. F. Yang, A. P. West, Jr., G. P. Allendorph, S. Choe, P. J. Bjorkman, Neogenin interacts with hemojuvelin through its two membrane-proximal fibronectin type III domains. *Biochemistry* **47**, 4237 (2008). doi:10.1021/bi800036h Medline

21. X. Landon, Cleavage at aspartyl-prolyl bonds. *Methods Enzymol.* **47**, 145 (1977). doi:10.1016/0076-6879(77)47017-4 Medline

22. C. Lanzara *et al*., Spectrum of hemojuvelin gene mutations in 1q-linked juvenile hemochromatosis. *Blood* **103**, 4317 (2004). doi:10.1182/blood-2004-01-0192 Medline

23. P. L. Lee, E. Beutler, S. V. Rao, J. C. Barton, Genetic abnormalities and juvenile hemochromatosis: mutations of the HJV gene encoding hemojuvelin. *Blood* **103**, 4669 (2004). doi:10.1182/blood-2004-01-0072 Medline

24. Materials and methods are available as supplementary materials on *Science* Online.

25. A. S. Zhang, A. P. West, Jr., A. E. Wyman, P. J. Bjorkman, C. A. Enns, Interaction of hemojuvelin with neogenin results in iron accumulation in human embryonic kidney 293 cells. *J. Biol. Chem.* **280**, 33885 (2005). doi:10.1074/jbc.M506207200 Medline

26. F. Yang, A. P. West, Jr., P. J. Bjorkman, Crystal structure of a hemojuvelin-binding fragment of neogenin at 1.8Å. *J. Struct. Biol.* **174**, 239 (2011). doi:10.1016/j.jsb.2010.10.005 Medline

27. X. Liu *et al*., Repulsive guidance molecule b inhibits neurite growth and is increased after spinal cord injury. *Biochem. Biophys. Res. Commun.* **382**, 795 (2009). doi:10.1016/j.bbrc.2009.03.115 Medline

28. K. Hata, K. Kaibuchi, S. Inagaki, T. Yamashita, Unc5B associates with LARG to mediate the action of repulsive guidance molecule. *J. Cell Biol.* **184**, 737 (2009). doi:10.1083/jcb.200807029 Medline

29. B. V. Geisbrecht, K. A. Dowd, R. W. Barfield, P. A. Longo, D. J. Leahy, Netrin binds discrete subdomains of DCC and UNC5 and mediates interactions between DCC and heparin. *J. Biol. Chem.* **278**, 32561 (2003). doi:10.1074/jbc.M302943200 Medline

30. J. P. Wong, E. Reboul, R. S. Molday, J. Kast, A carboxy-terminal affinity tag for the purification and mass spectrometric characterization of integral membrane proteins. *J. Proteome Res.* **8**, 2388 (2009). doi:10.1021/pr801008c Medline

31. A. R. Aricescu, W. Lu, E. Y. Jones, A time- and cost-efficient system for high-level protein production in mammalian cells. *Acta Crystallogr. D Biol. Crystallogr.* **62**, 1243 (2006). doi:10.1107/S0907444906029799 Medline

32. Y. Zhao *et al.*, Automation of large scale transient protein expression in mammalian cells. *J. Struct. Biol.* **175**, 209 (2011). doi:10.1016/j.jsb.2011.04.017 Medline

33. V. T. Chang *et al.*, Glycoprotein structural genomics: solving the glycosylation problem. *Structure* **15**, 267 (2007). doi:10.1016/j.str.2007.01.011 Medline

34. E. S. Trombetta, A. J. Parodi, Quality control and protein folding in the secretory pathway. *Annu. Rev. Cell Dev. Biol.* **19**, 649 (2003). doi:10.1146/annurev.cellbio.19.110701.153949 Medline

35. T. S. Walter *et al.*, A procedure for setting up high-throughput nanolitre crystallization experiments. Crystallization workflow for initial screening, automated storage, imaging and optimization. *Acta Crystallogr. D Biol. Crystallogr.* **61**, 651 (2005). doi:10.1107/S0907444905007808 Medline

36. Z. Otwinowski, W. Minor, Processing of X-ray diffraction data collected in oscillation mode. *Methods Enzymol.* **276**, 307 (1997). doi:10.1016/S0076-6879(97)76066-X

37. G. Winter, *xia2* : an expert system for macromolecular crystallography data reduction. *J. Appl. Cryst.* **43**, 186 (2010). doi:10.1107/S0021889809045701

38. A. J. McCoy, R. W. Grosse-Kunstleve, L. C. Storoni, R. J. Read, Likelihood-enhanced fast translation functions. *Acta Crystallogr. D Biol. Crystallogr.* **61**, 458 (2005). doi:10.1107/S0907444905001617 Medline

39. F. Yang, A. P. West, Jr., P. J. Bjorkman, Crystal structure of a hemojuvelin-binding fragment of neogenin at 1.8Å. *J. Struct. Biol.* **174**, 239 (2011). doi:10.1016/j.jsb.2010.10.005 Medline

40. M. D. Winn *et al.*, Overview of the CCP4 suite and current developments. *Acta Crystallogr. D Biol. Crystallogr.* **67**, 235 (2011). doi:10.1107/S0907444910045749 Medline

41. E. Blanc *et al.*, Refinement of severely incomplete structures with maximum likelihood in BUSTER-TNT. *Acta Crystallogr. D Biol. Crystallogr.* **60**, 2210 (2004). doi:10.1107/S0907444904016427 Medline

42. P. D. Adams *et al.*, PHENIX: building new software for automated crystallographic structure determination. *Acta Crystallogr. D Biol. Crystallogr.* **58**, 1948 (2002). doi:10.1107/S0907444902016657 Medline

43. P. Emsley, K. Cowtan, Coot: model-building tools for molecular graphics. *Acta Crystallogr. D Biol. Crystallogr.* **60**, 2126 (2004). doi:10.1107/S0907444904019158 Medline

44. G. J. Kleywegt, A. T. Brünger, Checking your imagination: applications of the free R value. *Structure* **4**, 897 (1996). doi:10.1016/S0969-2126(96)00097-4 Medline

45. I. W. Davis *et al*., MolProbity: all-atom contacts and structure validation for proteins and nucleic acids. *Nucleic Acids Res.* **35**, (Web Server), W375 (2007). doi:10.1093/nar/gkm216 Medline

46. D. I. Stuart, M. Levine, H. Muirhead, D. K. Stammers, Crystal structure of cat muscle pyruvate kinase at a resolution of 2.6 A. *J. Mol. Biol.* **134**, 109 (1979). doi:10.1016/0022-2836(79)90416-9 Medline

47. N. A. Baker, D. Sept, S. Joseph, M. J. Holst, J. A. McCammon, Electrostatics of nanosystems: application to microtubules and the ribosome. *Proc. Natl. Acad. Sci. U.S.A.* **98**, 10037 (2001). doi:10.1073/pnas.181342398 Medline

48. E. Krissinel, K. Henrick, Inference of macromolecular assemblies from crystalline state. *J. Mol. Biol.* **372**, 774 (2007). doi:10.1016/j.jmb.2007.05.022 Medline

49. C. A. O'Callaghan *et al*., BirA enzyme: production and application in the study of membrane receptor-ligand interactions by site-specific biotinylation. *Anal. Biochem.* **266**, 9 (1999). doi:10.1006/abio.1998.2930 Medline

50. P. Schuck, P. Rossmanith, Determination of the sedimentation coefficient distribution by least-squares boundary modeling. *Biopolymers* **54**, 328 (2000). doi:10.1002/1097-0282(20001015)54:5<328::AID-BIP40>3.0.CO;2-P Medline

51. P. H. Brown, P. Schuck, Macromolecular size-and-shape distributions by sedimentation velocity analytical ultracentrifugation. *Biophys. J.* **90**, 4651 (2006). doi:10.1529/biophysj.106.081372 Medline

52. R. J. Pasterkamp, J. J. Peschon, M. K. Spriggs, A. L. Kolodkin, Semaphorin 7A promotes axon outgrowth through integrins and MAPKs. *Nature* **424**, 398 (2003). doi:10.1038/nature01790 Medline

53. K. L. Bennett *et al*., Deleted in colorectal carcinoma (DCC) binds heparin via its fifth fibronectin type III domain. *J. Biol. Chem.* **272**, 26940 (1997). doi:10.1074/jbc.272.43.26940 Medline

54. B. V. Geisbrecht, K. A. Dowd, R. W. Barfield, P. A. Longo, D. J. Leahy, Netrin binds discrete subdomains of DCC and UNC5 and mediates interactions between DCC and heparin. *J. Biol. Chem.* **278**, 32561 (2003). doi:10.1074/jbc.M302943200 Medline

55. M. E. Lidell, G. C. Hansson, Cleavage in the GDPH sequence of the C-terminal cysteine-rich part of the human MUC5AC mucin. *Biochem. J.* **399**, 121 (2006). doi:10.1042/BJ20060443 Medline

56. M. E. Lidell, M. E. Johansson, G. C. Hansson, An autocatalytic cleavage in the C terminus of the human MUC2 mucin occurs at the low pH of the late secretory

pathway. *J. Biol. Chem.* **278**, 13944 (2003). doi:10.1074/jbc.M210069200 Medline

57. A. L. Ambrosio *et al*., Crossveinless-2 Is a BMP feedback inhibitor that binds Chordin/BMP to regulate Xenopus embryonic patterning. *Dev. Cell* **15**, 248 (2008). doi:10.1016/j.devcel.2008.06.013 Medline

58. J. E. Sadler, Biochemistry and genetics of von Willebrand factor. *Annu. Rev. Biochem.* **67**, 395 (1998). doi:10.1146/annurev.biochem.67.1.395 Medline

59. A. S. Zhang, A. P. West, Jr., A. E. Wyman, P. J. Bjorkman, C. A. Enns, Interaction of hemojuvelin with neogenin results in iron accumulation in human embryonic kidney 293 cells. *J. Biol. Chem.* **280**, 33885 (2005). doi:10.1074/jbc.M506207200 Medline